www.springer.com/41230
https://doi.org/10.1007/s41230-022-1192-1

Wear and corrosion resistance of CoCrNi composite coatings by laser cladding

Di Jiang[1], *Hong-zhi Cui[1,2], Xiao-jie Song[1], Xiao-juan Lian[1], Xiao-feng Zhao[1], Hao Chen[1], and Guo-liang Ma[1]

1. School of Materials Science and Engineering, Shandong University of Science and Technology, Qingdao 266590, China

2. School of Materials Science and Engineering, Ocean University of China, Qingdao 266100, China

Abstract: Two kinds of CoCrNi composite coatings, CoCrNiMo and CoCrNiMoBC, were prepared by laser cladding on the base metal of 304 stainless steel. The wear and corrosion properties of the coatings were studied by wear tests and electrochemical tests. Results show that the addition of B_4C promotes the generation of the ceramic phase, and therefore improving the microhardness of the coating and enhancing its wear resistance, while simutaneously keeps its excellent corrosion resistance. Energy dispersive X-ray spectrometry analysis shows that the chromium distribution in the two coatings is relatively uniform, which is beneficial for corrosion resistance. Scanning Kelvin probe microscopy results reveal that the potential difference between dendrites and interdendrites is only 20 mV, which leads to a relatively low driving force for galvanic corrosion. Observation through the atomic-scale high-resolution transmission electron microscopy shows that the fundamental reason for the high wear and corrosion resistance of the coating is the excellent coherent interface between the two phases, which reduces the interface energy and potential difference and thus improving its corrosion resistance.

Keywords: wear; corrosion; laser cladding; coherent boundary; 304 stainless steel

CLC numbers: TG146.1+6; Document code: A; Article ID: 1672-6421(2022)06-535-09

***Hong-zhi Cui**

Ph. D., Professor, Dean of the School of Materials Science and Engineering of Shandong University of Science and Technology from 2018 to 2021. Visiting scholar of Northwestern University in the United States from December 2013 to July 2014. Research interests: plasma, laser surface hardening, high flux marine abrasion and corrosion resistant coating technologies (material gene design).

Received: 2022-05-16
Accepted: 2022-10-23

1 Introduction

Wear, corrosion, and their interaction are inevitable failure modes of equipment used in marine environments [1]. Turbine blades, offshore drilling platforms, as well as various valves and drill pipes of desalination systems have always been corroded by seawater. Their surfaces gradually deteriorate under the action of stress and corrosion, which greatly shortens the service life and reduces the safety of the equipment [2]. Therefore, it is of great economic and social significance to develop materials with both high wear and high corrosion resistance [3].

Wear and corrosion resistance are opposing qualities and are difficult to obtain at the same time. Traditional marine steels, such as super duplex stainless steel 2205, 2207 [4, 5], super austenitic stainless steel 254SMO [6], and titanium alloys [7], are widely used in various marine equipment with excellent corrosion resistance, providing a reliable guarantee for safe operation. However, the hardness of these alloys is relatively low, and the surface is prone to serious wear from erosion and high stress, which leads to the damage of the passivation film. A great number of corrosive ions in seawater, such as from chloride ions and the local acidic environment, further intensify the corrosion, causing huge risks to the service safety of the equipment [8].

Ceramic strengthening is an important method for improving wear resistance [9]. The improved hardness can effectively resist external loads, avoiding plastic deformation, but at the same time, galvanic corrosion can be induced at the interface of different phases, resulting in reduced corrosion resistance [10]. Designing a suitable strengthening phase that can not only improve wear resistance but also maintain good corrosion resistance is a topic of focus.

In recent years, high-entropy alloys (HEAs) with equal atomic or nearly equal atomic ratios have become popular in the field of materials science [11]. Studies show that such alloys have excellent wear and corrosion resistance, good strength and toughness, and high temperature stability [12-15]. For example, the eutectic high-entropy alloy $FeCrNiCoNb_{0.5}$ with nanometer scale was prepared [16]. The results revealed that the nanometer scale eutectic structure is why the alloy has better corrosion resistance than 304SS. TiNbZr alloys with different amounts of Ag addition were prepared by arc melting, and an amorphous-nanocrystalline layer can be formed during wear tests, thus, protecting the alloy from further wear loss [17]. Moravcik et al. [18] studied the effects of N on the corrosion behavior of CoCrNi alloy in sulfuric acid solution, and pointed out that N element can effectively improve the pitting resistance of the alloy. Wang et al. [19] found Mo can also improve the corrosion resistance of CoCrFeNi alloy due to that with the addition of Mo, Cl^- can diffuse between Cr_2O_3 and MoO_3 in a more easier way, thus, minimize the attack on the metal surface. Among these HEAs, CoCrNi-based systems have been widely investigated because of their excellent comprehensive properties [21-25].

However, the size limit of arc melting, as well as the high cost, restricts the application of HEAs. A viable solution is to prepare protective HEA coatings on the surface of components. Laser cladding is a surface coating technique currently used in many industries [26-28]. This method can achieve good metallurgical bonding with the base metal to provide a high bonding strength that is suitable for various bearing and friction conditions. The high energy density and fast cooling speed of laser cladding can effectively reduce the grain size, improve the solid solubility of the system, while can also reduce the dilution rate and the heat-affected zone of the matrix to prevent deformation.

In this study, to prepare coatings with both high wear and high corrosion resistance, two different CoCrNi-based high-entropy alloy composite coatings, CoCrNiMo and CoCrNiMoBC, were prepared by laser cladding on 304 stainless steel (304SS), and their wear and corrosion resistance were studied. The correlations between the elemental distribution, microstructure and the wear and corrosion resistance of the coatings were analyzed.

2 Experimental procedures

2.1 Sample preparation

The nominal powder compositions of the two coatings are listed in Table 1. The size of the pure metal powder used was 50 μm in diameter (99.5wt.%), and B and C were added in B_4C particles (99.9wt.% purity) with an average diameter of 10 μm. The mixed powder was milled in a planetary muller for 5 h in alcohol under Ar protection and then dried in a vacuum at 50 °C. The laser power used for cladding was 1.4 kW, with a speed of 300 mm·min^{-1} under Ar protection to prevent oxidation. The base metal used was 304SS, and the thickness of the precoated powder was 2 mm.

Table 1: Nominal compositions of two coatings (at.%)

Samples	Co	Cr	Ni	Mo	B	C
CoCrNiMo	28.67	28.67	28.66	14	0	0
CoCrNiMoBC	27.00	27.00	27.00	14	4	1

2.2 Metallographic and microstructural analysis

The phase constitutions of the coatings were analyzed from 30° to 100° at a scanning rate of 4°·min^{-1} by X-ray diffraction (XRD, D/Max 2500 PC Rigaku, Japan) with Cu Kα radiation (λ=0.15405 nm). The microstructures of the coatings were examined using scanning electron microscopy (SEM). The chemical composition was analyzed with energy dispersive X-ray spectroscopy (EDS), and transmission electron microscopy (TEM) observations were conducted using a Thermol Fisher Scientific Talos F200X G2 TEM microscope operated at 200 kV. The TEM sample was prepared using the focused ion beam (FIB) technique (FEI Scios DualBeam).

2.3 Hardness, wear, and corrosion testing

The microhardness of the coatings from the top surface to the substrate was measured by using of a Vickers hardness tester (HV, ShiDai, HVS-1000) with a load of 2 N (200 g) and a duration time of 15 s.

Dry sliding tests were conducted on a reciprocating ball-on-plate tribometer (Rect MFT-5000, USA) with a normal load of 10 N for 30 min at a repeating frequency of 1 Hz. The counterpart was an Al_2O_3 ball with a diameter of 9.8 mm. The coefficient of friction (COF) was recorded simultaneously using the tester system, and the wear volume and morphology of the tracks were measured by 3D morphometry (BRUKER Contour GT-K1, Germany). The morphology of the worn surfaces was also evaluated by SEM.

The corrosion properties were evaluated using the three-electrode cells with a saturated calomel electrode (SCE) as the reference electrode, a platinum electrode as the auxiliary electrode, and a coating specimen as the working electrode. All electrochemical measurements were performed at room temperature (23±2 °C) and repeated at least three times to maintain reproducibility. The electrolyte solution was 3.5wt.% NaCl solution.

The potentiodynamic polarization of each sample was measured at a scanning rate of 0.5 mV·s^{-1} with a potential range from −0.2 V_{SCE} to a potential higher than the breakdown potential. Potentiostatic passivation was also tested for CoCrNiMo and CoCrNiMoBC at 0.2 V_{SCE} for 1 h to study the properties of the passive films. Then, electrochemical impedance spectroscopy (EIS) was conducted in the frequency range of 100 kHz–10 MHz. The experimental data were analyzed using the commercial software Gamry. Capacitance measurements were performed by sweeping the potential from an anodic value to a cathodic value, with a 10 mV AC signal and a step rate of 25 mV·s^{-1} at a frequency of 1,000 Hz. The sweeping rate employed was sufficiently fast to satisfy the assumption of a "frozen-in" defect structure for the Mott-Schottky theory [5]. Thus, the capacitance

reflected is the property of the electronic part of the space charge other than the ionic component in the film [29].

2.4 Scanning Kelvin probe force microscopy (SKPFM) measurements

The scanning Kelvin probe force microscopy (SKPFM) measurements of the polished samples were collected without etching. The probe used was a non-magnetized Cr/Pt conductive coating tip, and the resonance frequency of 60–90 kHz was used to map the volta potential variation between the phases. A dual-scan mode was used to record interactions in the electrostatic force in addition to the surface topography.

The topographies of the coating surfaces were obtained during the first scan. Then, the cantilever was lifted up by 100 nm to avoid the effects of topographic features on the potential mapping. An AC voltage was applied to the tip to oscillate the cantilever if an electric field between the tip and the sample surface was present. The oscillation of the cantilever was then nullified by applying a DC voltage to the tip. At this step, the potential of the tip and the sample surface were equal. The potential mapping of the sample surface can be acquired by this nullifying technique. The principle and details of the SKPFM measurements have been explained elsewhere [30].

3 Results and discussion

3.1 Phase analysis

The phase constitutions of the two coatings were identified by XRD, and the patterns are listed in Fig. 1. It can be seen the FCC solid solution is the main phase for both coatings, while $M_{23}(C,B)_6$ only exists in CoCrNiMoBC. In addition, σ formed in CoCrNiMo, which is consistant with the research results by Qin et al [31]. Notably, the preferential orientation is shown in the (200) of CoCrNiMoBC, while the (111) plane is preferred in CoCrNiMo. With the addition of B_4C, the intermetallic compound σ changes to form carbon boride because of the lower mixing enthalpy between metal atoms and boron/carbon.

3.2 Microstructural characterizations

Figure 2 presents the typical microstructures of the CoCrNiMo and CoCrNiMoBC coatings and the corresponding EDS results. As shown in Figs. 2(a, b), two structures can be seen: equiaxial grain and interdendritic structures. From the inset table in Fig. 2(b), it is clear that the equiaxial grain is rich in Co, Cr, and Ni, while the Mo content in the interdendritic area is much higher than the equiaxial grain. The elemental distributions are more noticeable in the EDS mapping, as shown in Fig. 2(c). Combining these findings with the XRD results, the interdendritic area can be determined to be σ, while the equiaxial grain is the FCC solid solution. The dendrite area is about 86%.

Figures 2(d, e) reveal the microstructure of the CoCrNiMoBC coating: typical dendritic and interdendritic structures. The dendrite structure is FCC rich in Co, Cr, and Ni, while the interdendritic region has more Cr, Mo, B, and C, which is determined to be $M_{23}(C,B)_6$. EDS mapping analysis in Fig. 2(f) also supports these findings. The dendrite area is about 62%.

The dendrite keeps the FCC structure upon adding 1at.% of B_4C, but with a much smaller size, whereas the interdendritic phase changes from σ to $M_{23}(C,B)_6$.

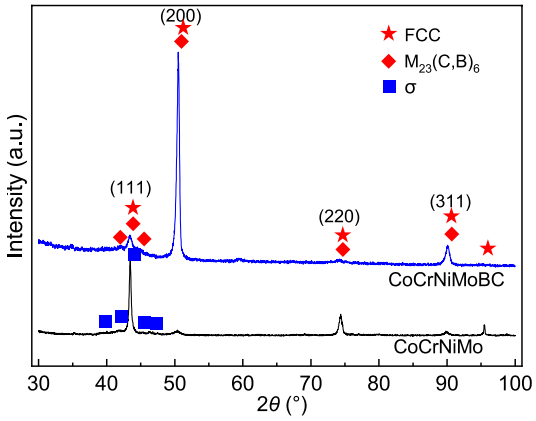

Fig. 1: X-ray diffraction patterns of two coatings

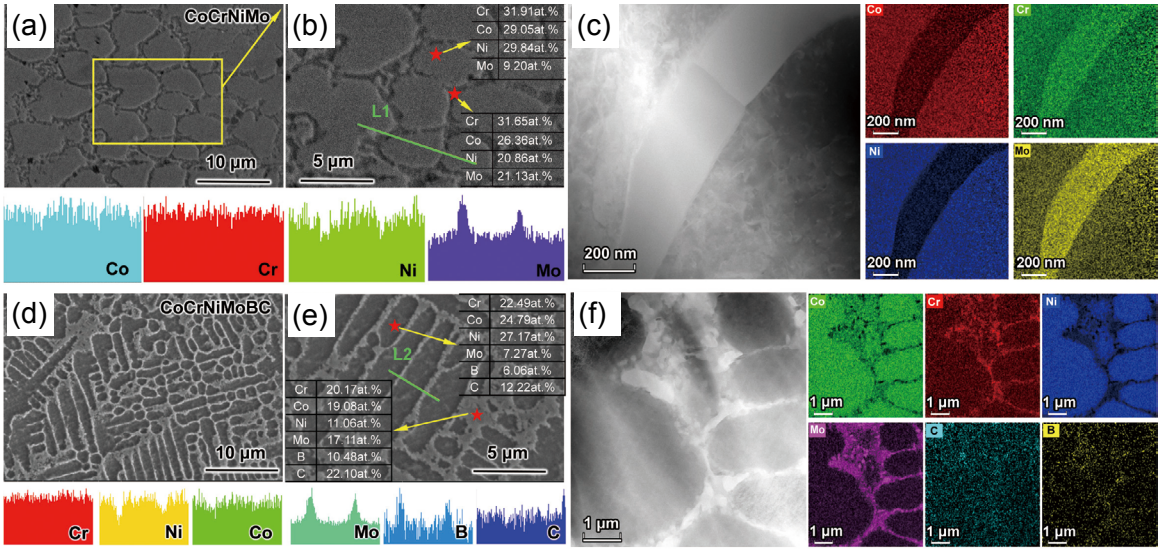

Fig. 2: SEM and TEM morphologies and EDS analysis of CoCrNiMo (a, b, c) and CoCrNiMoBC (d, e, f) coatings

3.3 Wear performance and analysis

Figure 3(a) shows the microhardness distribution along the depth of the coatings. The microhardness of the coatings is improved significantly upon adding 1at.% of B_4C in CoCrNiMo, reaching a maximum of 552 $HV_{0.2}$, almost three times that of the 304SS substrate. The hardness of CoCrNiMo is about 340 $HV_{0.2}$. The improvement in hardness comes from (1) the formation of the ceramic phase and (2) solid solution strengthening. From the COF curves, shown in Fig. 3(b), two different wear mechanisms can be inferred. The COF curve of CoCrNiMo is much more stable than that of CoCrNiMoBC even though their COFs are similar. Due to the relatively low hardness of CoCrNiMo, the friction pair easily intrudes into the coating, and no hard phases can provide enough resistance against plastic ploughing. So, during the reciprocating process, the resistance is much stable, leading to a stable COF curve. However, a great amount of ceramics form in CoCrNiMoBC coating, which can provide a great resistance to the movement of the friction pair, and cause the COF to gradually increase. However, these ceramics can be peeled off after applying friction several times, leading to the transient decrease in the COF before a subsequent cycle. Thus, a higher fluctuation is observed in Fig. 3(b). Figure 3(c) reveals the sectional profiles of the wear tracks. These sectional areas are greatly reduced due to the great improvement in the microhardness of CoCrNiMoBC. The wear volume in Fig. 3(d) also supports this conclusion.

Figure 4 shows the morphology of worn surface after wear tests. Two distinct characteristics can be observed. The CoCrNiMo coating with the lower hardness underwent severe plastic deformation under the force of the friction pair. The coating surface is ploughed and extruded leading to the formation of the patches and delamination. However, only fine furrows are seen on the worn surface of CoCrNiMoBC due to the improved hardness after the formation of the ceramic phase. As can also be seen from the 3D morphology, the depth of the worn track of CoCrNiMo is about 20 μm, which is two times that of CoCrNiMoBC, reflecting the significantly improved wear resistance of CoCrNiMoBC.

3.4 Electrochemical properties and passive film analysis

To evaluate the corrosion properties of the coatings, potential dynamic, potentiostatic polarization, and electrochemical impedance spectroscopy tests were performed in a 3.5wt.% NaCl solution. Figure 5(a) presents the potentiodynamic polarization results. The polarization kinetic parameters calculated from the curves are listed in the inset tables. These two coatings have almost the same E_{corr}, while the I_{corr} of CoCrNiMoBC being lower than that of CoCrNiMo. This indicates that CoCrNiMoBC has a lower corrosion rate than CoCrNiMo under open circuit potential conditions. Both coatings have a wide passive range of 0.9 V.

The point defect model (PDM) theory developed by Macdonald provides a satisfactory qualitative explanation for the growth and breakdown of the passivation films from a microscopic perspective [32-34]. The film can be treated as a bilayer with a highly disordered "barrier" layer adjacent to the metal, containing mostly metallic oxide and with an outer film comprised of a metallic hydroxide precipitated phase that may

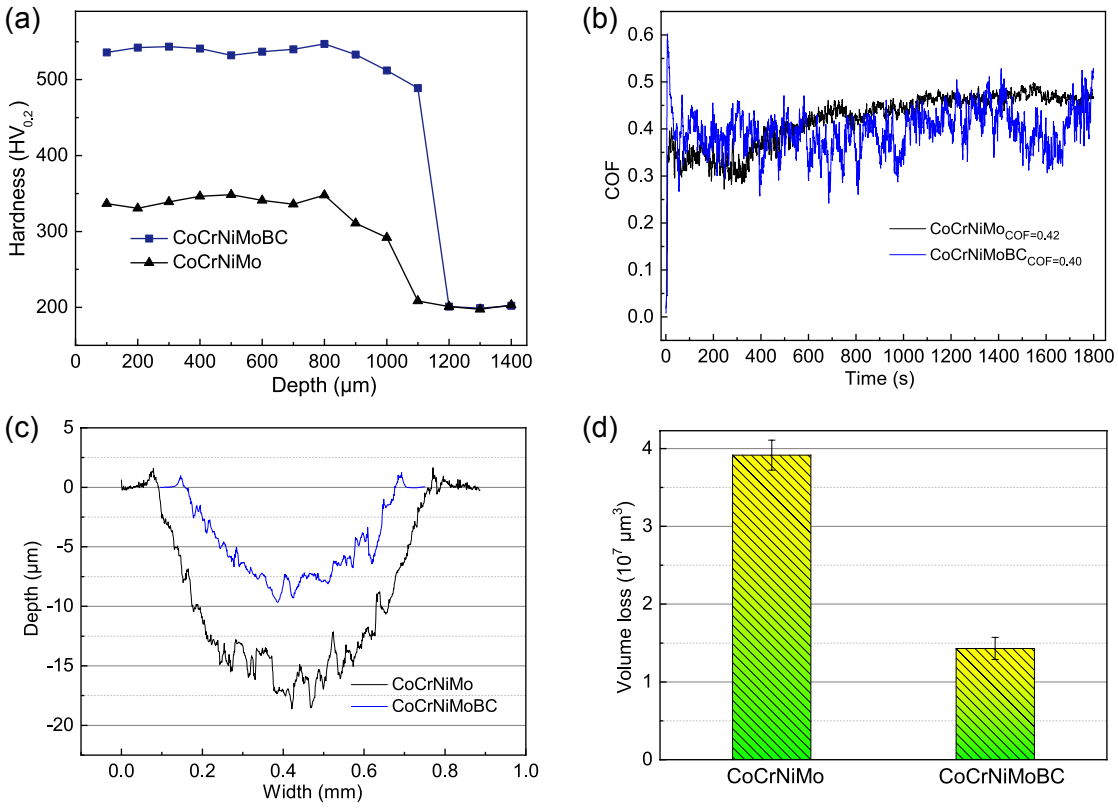

Fig. 3: Microhardness along depth of coatings (a), COF (b), wear sectional profiles (c), and wear volume loss (d)

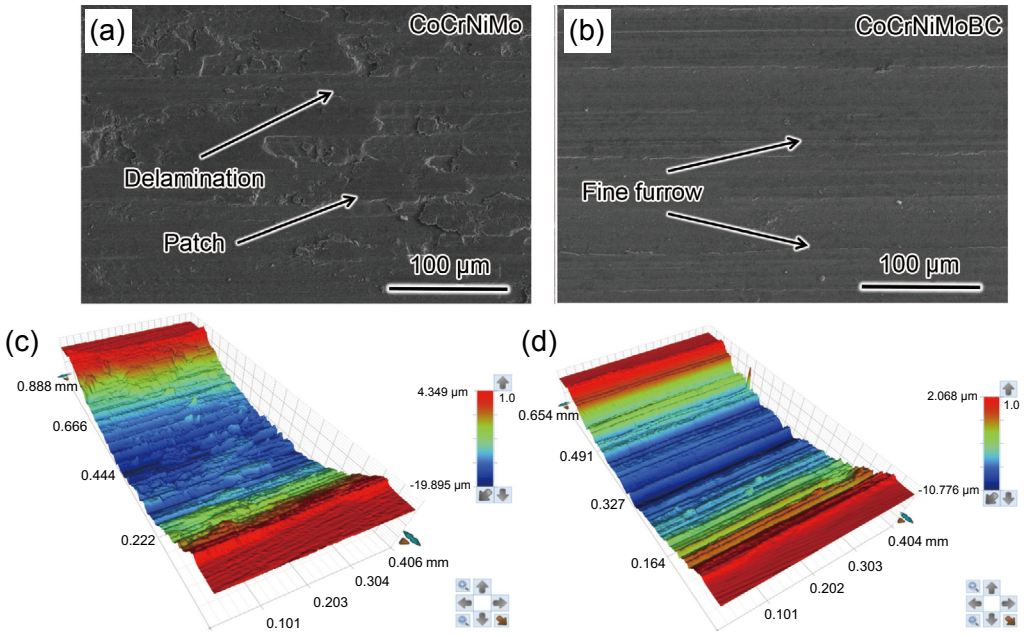

Fig. 4: SEM images (a, b) and 3D morphologies (c, d) of worn surfaces of CoCrNiMo (a, c) and CoCrNiMoBC (b, d)

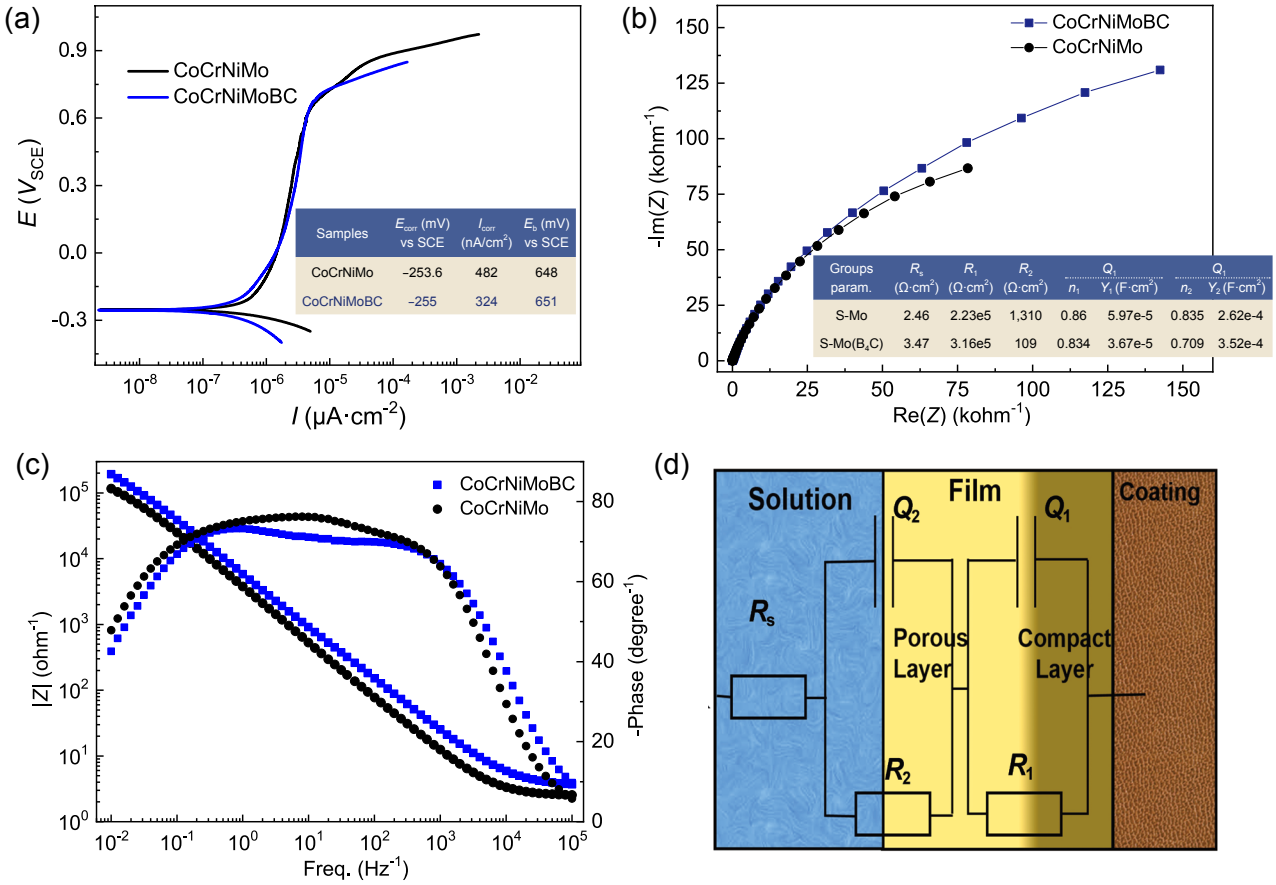

Fig. 5: Representative potentiodynamic polarization curves (a) and corresponding Nyquist plots (b); bode plots of passive films (c); equivalent circuits (d)

incorporate anions and/or cations from the solution. Therefore, a two-time constants model was used to reflect the inner and outer layers of the passivation films.

Figures 5(b, c) show the EIS results of the passive films under open circuit potential conditions based on the equivalent circuit indicated in Fig. 5(d). From the parameters shown in Fig. 5(b), CoCrNiMoBC has a greater charge transfer resistance, and therefore has better corrosion resistance. These findings imply that CoCrNiMoBC possesses better corrosion resistance than CoCrNiMo in NaCl solution.

In the circuit, R_s is the resistance of the solution, while R and Q are respectively the resistance and capacitance of the passive film (R_1 and Q_1 refer to the inner layer, and R_2 and Q_2 refer to the outer layer). The constant phase element (CPE) component is used to explain the non-ideal capacitance response of the film formed on the coatings caused by surface roughness and adsorption during EIS. The impedance (Z_{CPE}) of the non-ideal capacitance is given by [35]:

$$Z_{CPE} = Y^{-1}(j\omega)^{-n} \quad (1)$$

where Y is the proportional factor, ω is the angular frequency, and n is the CPE exponent associated with surface inhomogeneity from 0 to 1. Z_{CPE} represents a resistance with $R=Y^{-1}$ (n=0), an ideal capacitance with $C=Y$ (n=1), the Warburg element (n=0.5), or an inductance where $L=Y^{-1}$ (n=–1), L is the inductance. For the intermediate case where $0<n<1$, CPE can be correlated with the roughness. The general trend is that the lower the n, the rougher the corresponding electrode surface [36]. The n values of all the specimens are close to 1, indicating that the electrochemical behavior of the passive films is compact but different from the pure capacitive behavior.

The performance of passivation film is very important for the corrosion resistance of the coating. To further evaluate the corrosion resistance of both coatings, passivation films were prepared by electrostatic potential polarization at a potential of 0.2 V_{SCE}. The properties of the passivation films were tested with EIS and the Mott-Schottky method.

EIS curves for the passivation films are shown in Figs. 6(a, b). The resistance of CoCrNiMo is higher than CoCrNiMoBC, while both are much higher than that of the open circuit potential [Fig. 5(b)], indicating a better barrier property.

From the parameters listed in Table 2, it can be found that R_2 is relatively small because of the porous structure of the outer layer hydroxide. Therefore, only the inner layer film thickness was calculated using the following equation [37]:

$$d = \frac{\varepsilon\varepsilon_0 A}{C_{eff}} \quad (2)$$

where A is the surface area of the film; ε is the dielectric constant (equals to 15.6 in this case); and ε_0 is the vacuum permittivity (8.8542×10^{-14} F·cm^{-1}). C_{eff} is the effective capacitance of the passive film deduced from the CPE elements to interpret the properties of the film and can be expressed as:

$$C_{eff} = gQ(\rho_d \varepsilon\varepsilon_0)^{1-n} \quad (3)$$

In Eq. (3), the parameter ρ_d is the resistivity and can be assigned a value of 500 cm^2, while g is a function of n and can be expressed by the following equation:

$$g = 1 + 2.88(1-n)^{2.375} \quad (4)$$

The inner layer film thicknesses for CoCrNiMo and CoCrNiMoBC are 3.3 and 2.6 nm, respectively, and have a positive relationship with their resistances [38].

The electrical properties of the passive film on the coatings are important in understanding its protective characteristics against corrosion. According to the Mott-Schottky theory, a proven reasonable approach to calculating the donor density [39], the space charge capacitance (C) for a semiconductor electrode under the depletion conditions is given by Eq. (5) [40]:

$$\frac{1}{C^2} = \frac{2}{\varepsilon\varepsilon_0 e N_D}\left(E - E_{FB} - \frac{kT}{e}\right) \quad (5)$$

where N_D is the donor densities, e is the electron charge (1.6×10^{-19} C), k is the Boltzman constant (1.38×10^{-23} J·K^{-1}), T is the absolute temperature (K), E is the potential, and E_{FB} is the flat-band potential. As a result, the plot of C^{-2} versus E should be a straight line with a slope inversely proportional to the doping concentration. Figure 6(c) shows that both

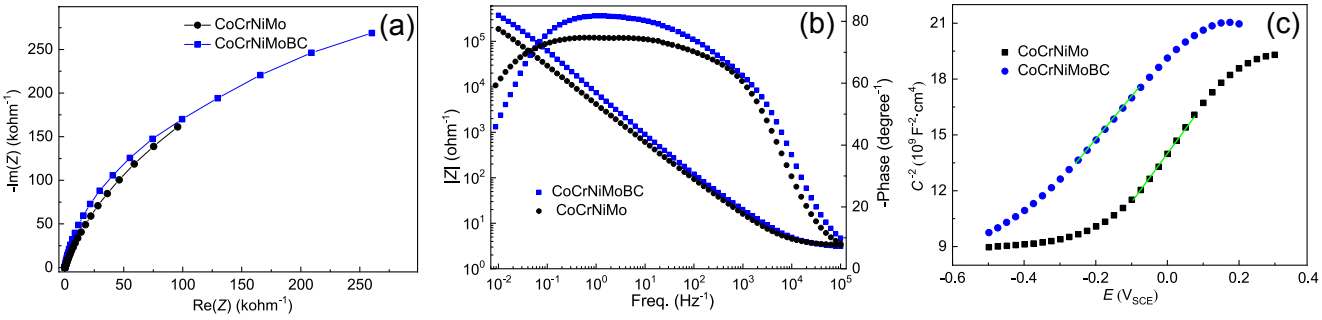

Fig. 6: Nyquist (a), Bode (b), and Mott-Schottky (c) plots of passive films obtained at 0.2 V_{SCE}

Table 2: Values of equivalent circuit elements for EIS data

Alloys	R_s (Ω·cm^2)	R_1 (Ω·cm^2)	R_2 (Ω·cm^2)	Q_1		Q_2		C_{eff} (F·cm^{-2})	d (nm)
				n_1	Y_1 (F·cm^{-2})	n_2	Y_2 (F·cm^{-2})		
CoCrNiMo	1.90	5.91e5	24.57	0.85	5.0e-5	0.62	0.0013	1.84e-6	3.3
CoCrNiMoBC	1.83	2.99e5	46.3	0.86	4.73e-5	0.42	0.0181	1.58e-6	2.9

the passivation film semiconductors are n-type (the slope is positive), meaning that the charge carriers are mainly oxygen vacancies or interstitial cations. However, although both the curves exhibit similar features, they are not straight because of the inhomogeneity of the films. The variation of the slope with the applied potential in this region is attributed to modifications of the passive film structure and composition. The parts chosen for line fitting are presented with green lines. The charge carrier densities of CoCrNiMo and CoCrNiMoBC were calculated according to Eq. (5) as 3.4×10^{20} and 4.1×10^{20} cm^{-3}, respectively.

3.5 Reasons for corrosion resistance improvement of CoCrNiMoBC coating

The wear resistance of CoCrNiMoBC was greatly improved compared with CoCrNiMo, while keeping a relatively high corrosion resistance. To figure out the mechanisms of its high corrosion resistance, the volta potential distribution of the coating was mapped using the scanning Kelvin probe force microscopy (SKPFM, Bruker Multimode 8). Figures 7(a, b) indicate the height and volta potential profiles of the same positions across different phases, and Fig. 7(c) is the profiles along the yellow lines in Figs. 7(a, b). Due to the relatively low potential difference between different phases, the contrast in Fig. 7(b) is not sufficiently clear. The potential difference along the line is in the range of 20 mV, which is quite small compared to other results [41-44]. Such a small potential difference can effectively reduce the driving force of galvanic corrosion, improve uniform corrosion, and enhance the corrosion resistance of the material [45].

To understand the reasons for the small potential difference between the two phases, TEM analysis was performed to explain this phenomenon from an atomic scale. Figures 8(a, b) show the SEM images of the FIB sample of CoCrNiMoBC before and after ion thinning, from which the grain and interdendritic region can be clearly seen. Figure 8(c) is the TEM bright field image. The HRTEM results of the interface between the two

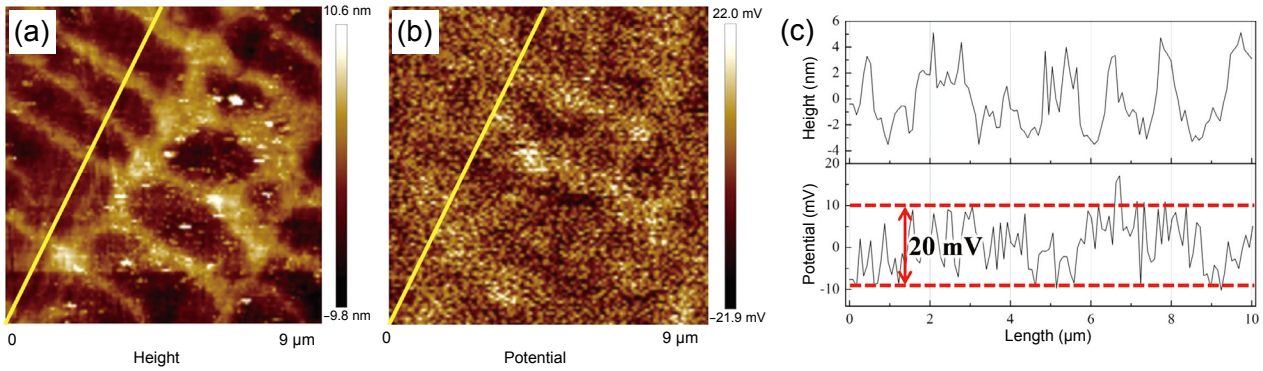

Fig. 7: Microstructure of CoCrNiMoBC (a), SKPFM image (b), and height and volta potential profiles along the marked yellow line (c)

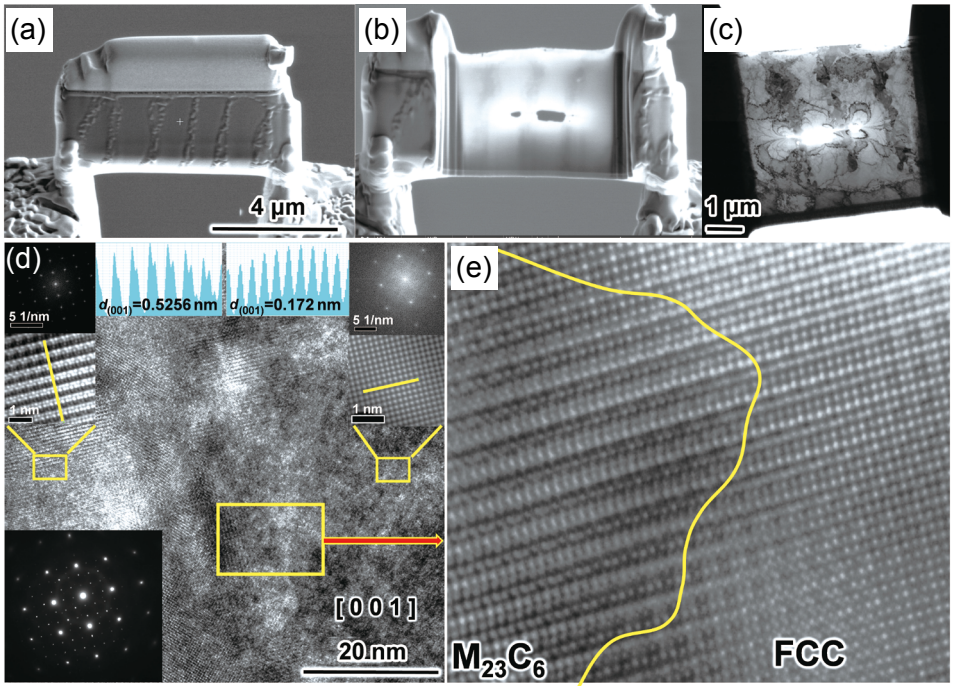

Fig. 8: Phase boundaries for CoCrNiMoBC: (a, b) SEM images of TEM samples; (c) bright-field image of TEM; (d) HRTEM image along [001] zone axis and corresponding FFT and IFFT images; (e) IFFT image of interface between the two phases

phases are shown in Fig. 8(d). Through selected area electron diffraction (SAED) of the [001] crystal axis, combined with XRD results, it can be seen that both phases have FCC lattice structure, with the lattice constant of $M_{23}(C,B)_6$ almost three times that of the FCC matrix. Figure 8(e) displays the inverse Fourier transform diagram at the interface, revealing that the two phases have a completely coherent interface without distortion. This completely coherent relation can effectively reduce the interfacial energy and internal stress of the system, which effectively reduces the potential difference between the two phases [46-47]. At the same time, the coherent interface can also ensure an excellent bonding force between the two phases, prevent interface cracking under the action of an external load, and promote the improvement of wear resistance [48].

4 Conclusions

In this study, two kinds of wear and corrosion resistant coatings were successfully prepared on the matrix metal of 304 stainless steel by laser cladding. With the addition of B_4C in CoCrNiMo, an optimal balance between wear and corrosion resistance can be realized. This strategy can be beneficial in the development of new materials serving for a harsh marine environments. Based on the analysis above, the major conclusions are obtained as follows:

(1) The CoCrNiMoBC coating has a better wear resistance than that of CoCrNiMo.

(2) With the introduction of B_4C, the wear resistance of the CoCrNiMoBC coating is greatly improved while keeping comparable corrosion resistance with CoCrNiMo coating.

(3) Results by scanning Kelvin probe force microscopy reveal that the potential difference between the dendritic and interdendritic areas of CoCrNiMoBC is only 20 mV.

(4) The ceramic $M_{23}(C,B)_6$ forms a fully coherent lattice with the FCC matrix, which is beneficial for the high wear and corrosion resistance of the CoCrNiMoBC coating.

Acknowledgements

The authors are grateful for the financial support of the National Natural Science Foundation of China (No. 51971121), the National Natural Science Foundation of China – Shandong Joint Fund for Marine Science Research Centers (CN) (No. U2106216), the Taishan Scholarship of Climbing Plan (No. tspd20161006), and the Major Special Science and Technology Projects in Shandong Province (Nos. 2019JZZY010303, 2019JZZY010360).

References

[1] Fu Y, Huang C, Du C, et al. Evolution in microstructure, wear, corrosion, and tribocorrosion behavior of Mo-containing high-entropy alloy coatings fabricated by laser cladding. Corros. Sci., 2021, 191: 109727–109738.

[2] Jiang D, Cui H, Chen H, et al. Wear and corrosion properties of B_4C-added CoCrNiMo high-entropy alloy coatings with in-situ coherent ceramic. Mater. Des., 2021, 210: 110068.

[3] Ureña J, Tsipas S, Pinto A M, et al. Corrosion and tribocorrosion behaviour of β-type Ti-Nb and Ti-Mo surfaces designed by diffusion treatments for biomedical applications. Corros. Sci., 2018, 140: 51–60.

[4] Cui Z, Chen S, Dou Y, et al. Passivation behavior and surface chemistry of 2507 super duplex stainless steel in artificial seawater: Influence of dissolved oxygen and pH. Corros. Sci., 2019, 150: 218–234.

[5] Cui Z, Wang L, Ni H, et al. Influence of temperature on the electrochemical and passivation behavior of 2507 super duplex stainless steel in simulated desulfurized flue gas condensates. Corros. Sci., 2017, 118: 31–48.

[6] Dou Y, Han S, Wang L, et al. Characterization of the passive properties of 254SMO stainless steel in simulated desulfurized flue gas condensates by electrochemical analysis, XPS and ToF-SIMS. Corros. Sci., 2020, 165: 108405.

[7] Zhang H, Man C, Dong C, et al. The corrosion behavior of Ti6Al4V fabricated by selective laser melting in the artificial saliva with different fluoride concentrations and pH values. Corros. Sci., 2021, 179: 109097.

[8] Wang J, Qian S, Li Y, et al. Passivity breakdown on 436 ferritic stainless steel in solutions containing chloride. J. Mater. Sci. Technol., 2019, 35: 637–643.

[9] Peng Y B, Zhang W, Li T C, et al. Microstructures and mechanical properties of FeCoCrNi high entropy alloy/WC reinforcing particles composite coatings prepared by laser cladding and plasma cladding. Int. J. Refract. Met. Hard Mater., 2019, 84: 105044.

[10] Shi Y, Yang B, Xie X, et al. Corrosion of Al_xCoCrFeNi high-entropy alloys: Al-content and potential scan-rate dependent pitting behavior. Corros. Sci., 2017, 119: 33–45.

[11] Qin G, Chen R, Mao H, et al. Experimental and theoretical investigations on the phase stability and mechanical properties of $Cr_7Mn_{25}Co_9Ni_{23}Cu_{36}$ high-entropy alloy. Acta Mater., 2021, 208: 116763.

[12] Ye Y X, Liu C Z, Wang H, et al. Friction and wear behavior of a single-phase equiatomic TiZrHfNb high-entropy alloy studied using a nanoscratch technique. Acta Mater., 2018, 147: 78–89.

[13] Han L, Rao Z, Souza F I R, et al. Ultrastrong and ductile soft magnetic high-entropy alloys via coherent ordered nanoprecipitates. Adv. Mater., 2021: 2102139.

[14] Zhao Y Y, Chen H W, Lu Z P, et al. Thermal stability and coarsening of coherent particles in a precipitation-hardened $(NiCoFeCr)_{94}Ti_2Al_4$ high-entropy alloy. Acta Mater., 2018, 147: 184–194.

[15] Alvi S, Akhtar F. High temperature tribology of CuMoTaWV high entropy alloy. Wear, 2019, 426–427: 412–419.

[16] Shuang S, Ding Z Y, Chung D, et al. Corrosion resistant nanostructured eutectic high entropy alloy. Corros. Sci., 2019, 164: 108315.

[17] Liu C, Li Z, Lu W, et al. Reactive wear protection through strong and deformable oxide nanocomposite surfaces. Nat. Commun., 2021, 12: 5518–5525.

[18] Moravcik I, Peighambardoust N S, Motallebzadeh A, et al. Interstitial nitrogen enhances corrosion resistance of an equiatomic CoCrNi medium-entropy alloy in sulfuric acid solution. Mater. Charact., 2021, 172: 110869.

[19] Wang W, Wang J, Sun Z, et al. Effect of Mo and aging temperature on corrosion behavior of $(CoCrFeNi)_{100-x}Mo_x$ high-entropy alloys. J. Alloys Compd., 2020, 812: 152139.

[20] Liang Y J, Wang L, Wen Y, et al. High-content ductile coherent nanoprecipitates achieve ultrastrong high-entropy alloys. Nat. Commun., 2018, 9: 4063.

[21] Zhao Y L, Yang T, Tong Y, et al. Heterogeneous precipitation behavior and stacking-fault-mediated deformation in a CoCrNi-based medium-entropy alloy. Acta Mater., 2017, 138: 72–82.

[22] Zhao Y, Yang T, Han B, et al. Exceptional nanostructure stability and its origins in the CoCrNi-based precipitation-strengthened medium-entropy alloy. Materials Research Letters, 2019, 7: 152–158.
[23] Moravcik I, Hadraba H, Li L, et al. Yield strength increase of a CoCrNi medium entropy alloy by interstitial nitrogen doping at maintained ductility. Scripta Mater., 2020, 178: 391–397.
[24] Liu X, Zhang M, Ma Y, et al. Achieving ultrahigh strength in CoCrNi-based medium-entropy alloys with synergistic strengthening effect. Mater. Sci. Eng. A, 2020, 776: 139028.
[25] Li N, Gu J, Gan B, et al. Effects of Mo-doping on the microstructure and mechanical properties of CoCrNi medium entropy alloy. J. Mater. Res., 2020, 35: 2726–2736.
[26] Cai Y, Zhu L, Cui Y, et al. Strengthening mechanisms in multi-phase FeCoCrNi$Al_{1.0}$ high-entropy alloy cladding layer. Mater. Charact., 2020, 159: 110037.
[27] Nair R B, Arora H S, Boyana A V, et al. Tribological behavior of microwave synthesized high entropy alloy claddings. Wear, 2019, 436-437: 203028.
[28] Zhao D, Yamaguchi T, Tusbasa D, et al. Fabrication and friction properties of the AlFeCrCo medium-entropy alloy coatings on magnesium alloy. Mater. Des., 2020, 193: 108872.
[29] Ahn S, Kwon H. Diffusivity of point defects in the passive film on Fe. J. Electroanal. Chem., 2005, 579: 311–319.
[30] Jacobs H O, Knapp H F, Miiller S, et al. Surface potential mapping – A qualitative material contrast in SPM. Ultmi, 1997, 69: 39–49.
[31] Qin G, Chen R, Zheng H, et al. Strengthening FCC-CoCrFeMnNi high entropy alloys by Mo addition. J. Mater. Sci. Technol., 2019, 35: 578–583.
[32] Macdonald D D. The point defect model for the passive state. J. Electrochem. Soc., 1992, 139: 3434–3449.
[33] Digby D M, Urquidi-Macdonald M. Theory of steady-state passive films. Journal Electrochemical Society, 1990, 137: 2395–2402.
[34] Macdonald D D, Biaggio S R, Song H. Steady-state passive films. Journal Electrochemical Society, 1992, 139: 170–177.
[35] Yen C C, Lu H N, Tsai M H, et al. Corrosion mechanism of annealed equiatomic AlCoCrFeNi tri-phase high-entropy alloy in 0.5 M H_2SO_4 aerated aqueous solution. Corros. Sci., 2019, 157: 462–471.
[36] Guo Y, Li C, Zeng M, et al. In-situ TiC reinforced CoCrCuFeNi$Si_{0.2}$ high-entropy alloy coatings designed for enhanced wear performance by laser cladding. Mater. Chem. Phys., 2020, 242: 122522.
[37] Orazem M E, Frateur I, Tribollet B, et al. Dielectric properties of materials showing constant-phase-element (CPE) impedance response. J. Electrochem. Soc., 2013, 160: C215–C225.
[38] Feng Z, Cheng X, Dong C, et al. Passivity of 316L stainless steel in borate buffer solution studied by Mott–Schottky analysis, atomic absorption spectrometry and X-ray photoelectron spectroscopy. Corros. Sci., 2010, 52: 3646–3653.
[39] Zhang M, Zhou X, Yu X, et al. Synthesis and characterization of refractory TiZrNbWMo high-entropy alloy coating by laser cladding. Surf. Coat. Technol., 2017, 311: 321–329.
[40] Wang F, Inoue A, Kong F L, et al. Formation, stability and ultrahigh strength of novel nanostructured alloys by partial crystallization of high-entropy $(Fe_{0.25}Co_{0.25}Ni_{0.25}Cr_{0.125}Mo_{0.125})_{86\text{-}89}B_{11\text{-}14}$ amorphous phase. Acta Mater., 2019, 170: 50–61.
[41] Zheng S, Li C, Qi Y, et al. Mechanism of (Mg, Al, Ca)-oxide inclusion-induced pitting corrosion in 316L stainless steel exposed to sulphur environments containing chloride ion. Corros. Sci., 2013, 67: 20–31.
[42] Sarvghad-Moghaddam M, Parvizi R, Davoodi A, et al. Establishing a correlation between interfacial microstructures and corrosion initiation sites in Al/Cu joints by SEM-EDS and AFM-SKPFM. Corros. Sci., 2014, 79: 148–158.
[43] Fuertes N, Pettersson R. Review – Passive film properties and electrochemical response of different phases in a Cu-alloyed stainless steel after long term heat treatment. J. Electrochem. Soc., 2016, 163: C377–C385.
[44] Depentori F, Forcellini C, Andreatta F, et al. Oxidation of neodymium precipitates in a $Ti_6Al_4V_2Nd$ alloy in sodium chloride solution. Mater. Corros., 2016, 67: 277–285.
[45] Zhang H W, Man C, Wang L W, et al. Different corrosion behaviors between α and β phases of Ti_6Al_4V in fluoride-containing solutions: Influence of alloying element Al. Corros. Sci., 2020, 169: 108605.
[46] Zhang M X, Kelly P M. Edge-to-edge matching and its applications. Acta Mater., 2005, 53: 1073–1096.
[47] Kelly P M, Zhang M X. Edge-to-edge matching – The fundamentals. Metall. Mater. Trans. A., 2006, 36: 833.
[48] Wang M, Cui H, Wei N, et al. A new design of in situ Ti(C, N) reinforced composite coatings and their microstructures, interfaces, and wear resistances. ACS, Appl, Mater. Inter., 2018, 10: 4250–4265.